High-performance flexible all-solid-state asymmetric supercapacitors based on binder-free MXene/cellulose nanofiber anode and carbon cloth/polyaniline cathode

Xiaoyu Bi[1], Meichun Li[2], Guoqiang Zhou[1], Chaozheng Liu[1], Runzhou Huang[1] (✉), Yang Shi[1], Ben Bin Xu[3], Zhanhu Guo[3] (✉), Wei Fan[4], Hassan Algadi[3,5,6], and Shengbo Ge[1] (✉)

[1] Jiangsu Co-Innovation Center of Efficient Processing and Utilization of Forest Resources, International Innovation Center for Forest Chemicals and Materials, College of Materials Science and Engineering, Nanjing Forestry University, Nanjing 210037, China

[2] School of Petroleum Engineering, China University of Petroleum (East China), Qingdao 266580, China

[3] Integrated Composites Lab, Department of Mechanical and Construction Engineering, Northumbria University, Newcastle Upon Tyne, NE1 8ST, UK

[4] School of Textile Science and Engineering & Key Laboratory of Functional Textile Material and Product of Ministry of Education, Xi'an Polytechnic University, Xi'an 710048, China

[5] College of Materials Science and Engineering, Taiyuan University of Science and Technology, Taiyuan 030024, China

[6] Department of Electrical Engineering, Faculty of Engineering, Najran University, Najran, 11001, Saudi Arabia

ABSTRACT

The search for wearable electronics has been attracted great efforts, and there is an ever-growing demand for all-solid-state flexible energy storage devices. However, it is a challenge to obtain both positive and negative electrodes with excellent mechanical strength and match positive and negative charges to achieve high energy densities and operate voltages to satisfy practical application requirements. Here, flexible MXene ($Ti_3C_2T_x$)/cellulose nanofiber (CNF) composite film negative electrodes (MCNF) were fabricated with a vacuum filtration method, as well as positive electrodes (CP) by combining polyaniline (PANI) with carbon cloth (CC) using an *in-situ* polymerization method. Both positive and negative free-standing electrodes exhibited excellent electrochemical behavior and bendable/foldable flexibility. As a result, the all-pseudocapacitance asymmetric device of MCNF//CP assembled with charge-matched between anode and cathode achieves an extended voltage window of 1.5 V, high energy density of 30.6 Wh·kg⁻¹ (1211 W·kg⁻¹), and 86% capacitance retention after 5000 cycles, and the device maintains excellent bendability, simultaneously. This work will pave the way for the development of all-pseudocapacitive asymmetric supercapacitors (ASC) with simultaneously preeminent mechanical properties, high energy density, and wide operating voltage window.

KEYWORDS

MXene, cellulose nanofiber, polyaniline, asymmetric supercapacitors

1　Introduction

Supercapacitors (SCs) are energy storage devices with broad application prospects, which have the characteristics of high power density, fast charging and discharging speed, and long cycle life [1]. However, in addition to the above properties, excellent flexibility and high energy density (*E*) are also necessary for the rapidly developing wearable electronic devices, photovoltaic energy storage systems, and other industries [2–5]. According to the equation $E = \frac{1}{2}CV^2$, higher specific capacity (*C*) and wider operating voltage window (*V*) are the prerequisites to improve the energy density of the device, and the selection of high performance positive and negative electrodes for charge matching to assemble asymmetric SCs (ASCs) is a proven strategy to improve the *E* [6–8]. Moreover, the addition of binders (e.g., polytetrafluoroethylene and polyvinylidene fluoride) and

conductive agents (e.g., carbon black) in conventional electrodes not only reduces the mass ratio of active substances in the whole electrode, but also greatly increases the volume and weight [9, 10]. On the other hand, flexible devices have high requirements for repeated bending and portability, and the poor strength of free-standing electrode or the weak bonding between electrode material and substrate can make device difficult to be applied in practice [11–14]. Therefore, there is a crucial need for the development of positive and negative pseudocapacitive electrode materials with both extraordinary electrochemical performance, flexibility and wear resistance to assemble ASCs with practical applications [15, 16].

MXene, a family of two-dimensional (2D) transition-metal carbides and nitrides material, has been known for its high pseudocapacity, metallic conductivity, and modifiable surface-

---

terminating moieties, and has attracted a lot of attention in the field of flexible energy storage devices [17–19]. Unlike graphene, which has a natural 2D structure, MXene is formed by selectively removing the Al-layer in the MAX phase to form a 2D lamellar structure, whose structural formula can be expressed as $M_{n+1}X_nT_x$, where M_{n+1} is an early transition metal (Mo, Ti, and Nb), X_n is C or N, and T_x represents a surface functional group (–O, –OH, and –F) [20]. The abundant surface functional groups endow the material hydrophilicity and enable it to be dispersed into a homogeneous and stable aqueous solution, which is conducive to further processing (such as spin coating, vacuum filtration, freeze-drying, etc.) [21–23]. The application of $Ti_3C_2T_x$ MXene, carbon materials such as porous carbon, carbon nanotubes, and graphene, and conducting polymers such as polypyrrole and polyaniline (PANI) to positive and negative electrode materials has been widely reported [24–28]. However, practical structural materials for flexible electronics that combine both the high capacitance and mechanical strength required are still rare and the fabrication of the electrodes is full of challenge [29]. Cellulose nanofiber (CNF), as a kind of nanomaterials from green, low-cost, abundant, renewable, and biodegradable natural resources., has a high aspect ratio and mechanical strength [30, 31]. Inspired by the "brick-and-mortar" architecture of nacres, combining CNF with MXene as a binder not only does not significantly affect the original flexibility and electrochemical properties of MXene due to its own structure, but also significantly improves the mechanical properties, which is a viable strategy for the preparation of flexible devices [32]. CNF can be mixed with MXene to form a uniform and stable colloidal suspension, and the hybrid films fabricated with colloidal solution by vacuum filtration method can maintain excellent continuous channels between the MXene sheet structures to guarantee ion transfer and charge diffusion without changing the pseudocapacitive energy storage mechanism on the material surface, effectively maintaining the specific capacitance of the electrodes [33].

MXene exhibits irreversible oxidization at excessively high anode potentials, which leads to a largely restricted operating voltage window for most of the MXene-based symmetric supercapacitors under current study [34]. Among various positive electrode materials, PANI is one of the most widely used conductive polymers, owing to its advantages of high specific capacitance, easy synthesis, low-cost, and good environment stability [35, 36]. For instance, Li and co-workers synthesized the MXene/PANI electrode material using hydrothermal method and reported a high specific capacitance of 563 F·g⁻¹ and excellent rate capability (current density range from 0.5 to 20 A·g⁻¹, 84.72%) [37]. The repeated expansion and contraction of PANI during long-term charge/discharge cycles dramatically delaminated its rate capability and cycle life, so it is crucial to find an appropriate substrate [38]. Conventional electrode preparation requires combining active material, binder, and conductive agent with the substrate. This sacrifices the flexibility of the electrode, meanwhile, the addition of polymeric binder causes some of the active materials to agglomerate, which will not expose all the reactive sites, thus reducing the ion diffusion efficiency and ultimately deteriorating the specific capacitance [39]. The commercially available carbon cloth (CC) has outstanding electrical conductivity, high specific surface area, and porous structure, which is particularly favorable for electrode active materials to be coated or polymerized on the surface, while the promising mechanical properties also gift CC significant potential for application in the field of flexible energy storage devices [40, 41]. The nanostructured PANI is uniformly and intensively polymerized on the surface of carbon textile fibers to ensure superior ion diffusion efficiency, and the flexible CC fibers can

provide strong interfacial adhesion while also act as an elastic buffer to accommodate the swelling and shrinking of PANI backbone during charging and discharging process, which is conducive to extending cycle life [42]. Ahirrao and co-workers used an *in-situ* chemical oxidation polymerization method to cover PANI uniformly on the CC surface, and the composite electrode exhibited a positive potential operating voltage of 0–0.8 V in a 1 M sulfuric acid electrolyte, obtained a high specific capacitance of up to 691 F·g⁻¹ at a current density of 1 A·g⁻, and exhibited an excellent cycling stability of 94% at 2000 times constant current charge and discharge [43].

Herein, in this study, a wearable, foldable free-standing energy storage device was assembled by combining two kinds of high-performance flexible electrode materials. Both demonstrated high-rate capability and pseudocapacitance, in which functional groups on the surface of MXene/cellulose nanofiber (MCNF) and positive electrodes (CP) involved in the redox reaction on the positive and negative electrodes, respectively. The negative electrode was prepared by combining CNF uniformly with MXene nanosheets using a simple vacuum filtration self-assembly method, and the positive electrode was manufactured by densely growing aniline (ANI) on the surface of each single fiber of the CC textile via chemical *in-situ* polymerization method to produce CP electrode. Both methods of electrode fabrication are simple, valid implementation, and low-cost for MCNF//CP ASCs, and the charge matching ($Q^+ = Q^-$) can be easily balanced by curbing PANI polymerization time or MXene mass loading. The device exhibits an operating voltage window of up to 1.5 V, a gravimetric E of 30.6 Wh·kg⁻¹ (1211 W·kg⁻¹) and ultralong lifespan of 86% after 5000 cycles. Meanwhile, the balance of high flexibility, bendability, and electrochemical performance of ASCs demonstrates potential applications for wearable smart electronics.

2 Materials and methods

2.1 Materials

Layered ternary carbide (Ti_3AlC_2, MAX) powders were purchased from Foshan Xinxi Technology Co., Ltd. (Guangzhou, China). Hydrochloric acid (HCl, 35%–38%), lithium fluoride (LiF, 99%), ANI, ammonium persulphate (APS), and sulfuric acid (H_2SO_4) were purchased from Aladdin Reagent Co., Ltd. The CNFs (2.5 wt.% concentration) were provided by Zhongshan NanoFC Co., Ltd. (Guangdong, China).

2.2 Preparation of delaminated $Ti_3C_2T_x$

$Ti_3C_2T_x$ was fabricated by selectively etching Al species from the MAX phase. First, 2.8 g of LiF powder was dissolved in 40 mL of 9 M HCl acid solution and stirred for 15 min at room temperature to prepare etching solution. When the solution became stable, 2 g Ti_3AlC_2 powders (400 mesh) were slowly added to the LiF/HCl solution followed by magnetic stirring for 36 h at 35 °C. Further, the resultant stable suspension was repeatedly washed using deionized water and centrifuged (3500 rpm, 5 min) until the pH was higher than 6. The obtained deposit was redispersed in deionized water and sonicated for 30 min in an ice-water bath under argon gas bubbles below the liquid level. Finally, after centrifugation for one hour at 3500 rpm, the delaminated $Ti_3C_2T_x$ suspension was obtained by collecting the dark green supernatant (≈ 1 mg·mL⁻¹).

2.3 Preparation of MCNF free-standing films

$Ti_3C_2T_x$/CNF hybrid dispersions were prepared by adding different amount of CNF water dispersion (from 0 wt.% to 16 wt.%) into the same volume of $Ti_3C_2T_x$ dispersion (35 mL,

1 mg·mL^{-1}). Ti$_3$C$_2$T$_x$/CNF nanopapers were fabricated through simple vacuum filtration of the mixture on a Celgard 3501 filter membrane with a pore size of 0.25 μm, smaller than the length of one-dimensional (1D) CNF and the lateral size of 2D MXene Ti$_3$C$_2$T$_x$ in the hybrid dispersion to obtain a free-standing film. Finally, the Ti$_3$C$_2$T$_x$/CNF hybrid film was peeled off and dried in a vacuum system for further use. The hybrid films are labeled as MCNF-*X*, where *X* is the weight percentage of CNF in the nanopaper. The thickness of the obtained nanopapers was ~ 6 μm for pristine Ti$_3$C$_2$T$_x$, and ~ 8, 10, and 13 μm for the films with 4%, 8%, and 16% CNF loading, respectively.

2.4 Preparation of CP electrode

The CC/PANI composites electrode was synthesized by *in-situ* chemical oxidative polymerization of aniline monomer on CC substrate. CC (1 cm^{-1} × 2 cm^{-1}) was first dipped in H$_2$SO$_4$/HNO$_3$ solution to perform the activation treatment and then sequentially cleaned by ultrasound in deionized water and ethanol to remove impurities followed by air drying. 1 mL of ANI and 2.5 g of APS were added to 50 mL of 1 M HCl, respectively, both of which were carried out in an ice bath. Then, the CC was soaked in the mixed solution of ANI/HCl for 30 min to make it fully infiltrated, which is conducive to the uniform polymerization of aniline on the surface of the CC. To start the polymerization, APS solution was added very slowly into the CC/ANI/HCl solution at 0–5 °C for 6–8 h. Finally, PANI coated CC substrate was washed with DI water and ethanol to remove the unreacted monomers and loosely bound PANI from the CC surface.

As obtained CP composite and PANI powder were dried oven overnight at 60 °C for further use. The amount of PANI decorated on the CC substrate was calculated by weighing the CC before and after the polymerization reaction.

2.5 Fabrication of solid-state MCNF//CP asymmetric device

The polyvinyl alcohol (PVA) solution was fabricated by adding 2 g of PVA powder into 20 mL of DI water with continuous stirring at 90 °C until the PVA was complete transparent. Afterward, 1 mL H$_2$SO$_4$ was added to the above transparent solution and stirred vigorously for 30 min. The mixture electrolyte was drop-casted onto a clear glass. Then a solid-state asymmetric device was manufactured by using the CP as the anode and MCNF as the cathode with PVA/ H$_2$SO$_4$ gel directly serving as the separator and electrolyte between both electrodes. The charge match between the cathode and anode can be well balanced by controlling the polymerization time of the CC in the ANI/HCl mixture, the amount of active materials on the substrate was controlled.

2.6 Characterizations

The morphology and microstructure of the samples were captured using transmission electron microscopy (TEM, JEM-1400 UHR), high-resolution TEM (HR-TEM, JEM-2100 UHR), and a field-emission scanning electron microscopy (FE-SEM, Regulus 8100) with an energy dispersive spectroscopy (EDX). The chemical structure of the composite was measured by an X-ray diffractometer (XRD, Ultima IV) with a radiation source of Cu Kα at 40 kV and 30 mA. Further, the diffractometer was operated at a scan speed of 0.05 °·min^{-1} within a 2θ range of 3°–80°. The surface chemical compositions and bonding states were detected by X-ray photoelectron spectroscopy (XPS, AXIS UltraDLD) with an Al Kα X-ray source, which was performed at 15 kV, 10 mA, and 160 eV (for the survey scan mode) or 40 eV (for the high-resolution scan mode, e.g., C 1s, N 1s, O 1s, and Ti 2p). The CASAXPS software was used for analyzing the chemical bonding states by

deconvoluting the obtained high-resolution spectra. Fourier transform infrared (FTIR) spectroscopy of the samples was recorded using FTIR spectrometer (FTIR, VERTEX 80 V) in the wavenumber range of 500–4000 cm^{-1} with a resolution of 4 cm^{-1} at room temperature.

All electrochemical testing was performed on a CHI 760E electrochemical workstation (Chenhua, Shanghai, China). The electrochemical performance of single electrodes was characterized in a three-electrode configuration with 1 M H$_2$SO$_4$ as aqueous electrolyte where a glassy carbon electrode was used as the counter electrode and Ag/AgCl in saturated KCl was used as reference electrode. The electrochemical performance of single electrode and asymmetric device was evaluated by cyclic voltammetry (CV), galvanostatic charge–discharge (GCD), and electrochemical impedance spectroscopy (EIS). The EIS test was performed at an open circuit potential at an amplitude of 5 mV and in a frequency range from 10^{-2} to 10^3 kHz. The long-term cycling stability was evaluated by conducting the GCD test for 5000 cycles at a current density of 20A·g^{-1}.

2.7 Capacitance and energy density calculations

The specific capacitance of single electrodes was calculated from the discharge portion of CV curves according to the Eq. (1)

$$C_g = \frac{\int I dV}{mv\Delta V} \tag{1}$$

where C_g is the gravimetric capacitance (F·g^{-1}), I is the current (A), ΔV is the potential window (V), m is the amount of the active materials (g), and v is the scan rate (mV·s^{-1}), respectively.

The areal capacitance (C_A) was calculated according to Eq. (2)

$$C_A = \frac{mC_g}{a} \tag{2}$$

where a is the area of one electrode (cm^{-2}).

The gravimetric capacitance and areal capacitance of asymmetric devices were calculated from the discharge portion of CV curves according to Eqs. (3) and (4)

$$C_G = \frac{\int I dV}{Gv\Delta V} \tag{3}$$

$$C_A = \frac{GC_G}{A} \tag{4}$$

where G is the total mass of positive and negative electrodes (g) and A is the geometric area of the electrode material (cm^{-2}).

The charge match between the cathode and anode (q$^+$ = q$^-$) is calculated according to Eq. (5)

$$\frac{m^+}{m^-} = \frac{C_g^- \Delta V^-}{C_g^+ \Delta V^+} \tag{5}$$

The gravimetric energy density (Wh·kg^{-1}) and gravimetric power density (kW·kg^{-1}), based on asymmetric supercapacitor, were calculated according to the following equations

$$E = \frac{1}{7.2} C_g V^2 \tag{6}$$

$$P = \frac{3600E}{\Delta t} \tag{7}$$

where Δt is the discharge time (s).

3 Results and discussion

Figure 1 schematically illustrates the design of the asymmetric supercapacitor with MCNF and CP as the negative and positive
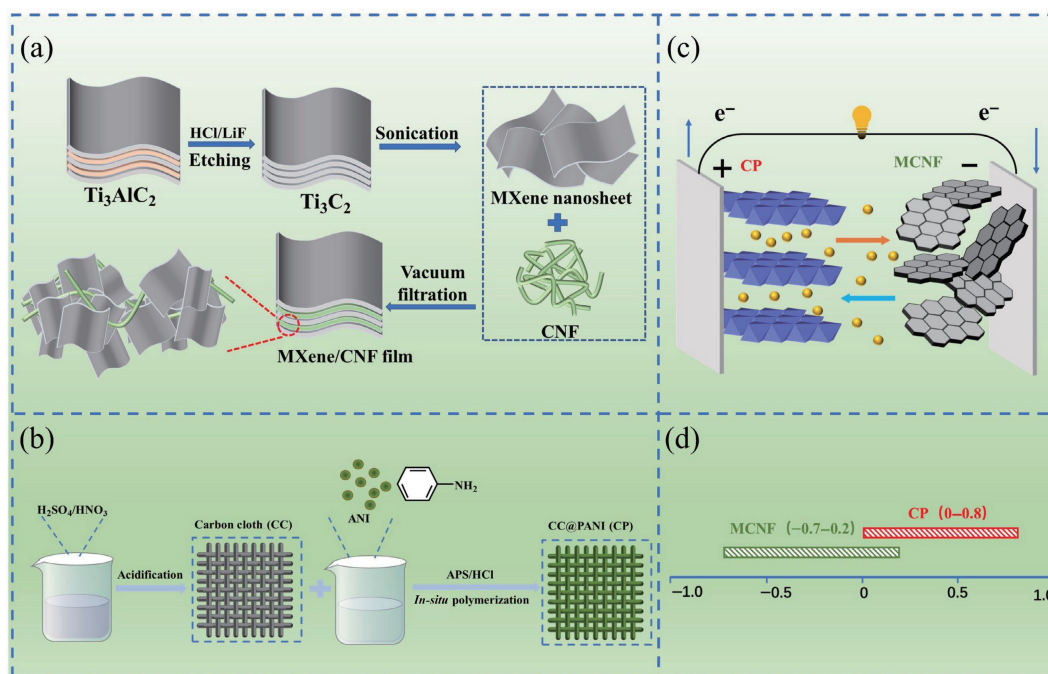
Figure 1 Fabrication process of Ti$_3$C$_2$T$_x$ MXene/CNF and CP (carbon cloth/PANI) electrode and schematic illustration of the all-pseudocapacitive asymmetric supercapacitor. (a) and (b) Synthesis scheme of MCNF and CP electrode, (c) schematic illustration of asymmetric supercapacitor, in which CP and MCNF serve as the positive and negative electrode, respectively, and (d) the working potential window of MCNF and CP in a three-electrode aqueous electrolyte system.

electrode, respectively. For the preparation of the negative electrode, the aluminum atomic layer of MAX phase was firstly removed via HCl/LiF etching solution, and then the CNF (0.2 wt.%) solution was mixed uniformly with MXene colloid solution through ultrasonic treatment before vacuum filtration, and the MCNF free-standing nanopaper electrode was peeled off from membrane after vacuum drying (Fig. 1(a)). For the fabrication of the positive electrode, the CC was dipped in H$_2$SO$_4$/HNO$_3$ to perform the activation treatment, and the fully cleaned CC was pre-soaked in a mixture of ANI/HCl solution, then APS was slowly added to initiate the polymerization reaction, and PANI was uniformly covered on each carbon fabric fiber, thus the flexible CP positive electrode is obtained (Fig. 1(b)). Figure 1(c) is the schematic representation of the all-pseudocapacitive asymmetric device where MCNF and CP are the negative and positive electrode, respectively. Figure 1(d) depicts the operating voltages window of MCNF negative and CP positive electrodes tested in a three-electrode system in 1 M H$_2$SO$_4$ as the electrolyte, respectively, and the assembled devices are obtained with a wide voltages window at 1.5 V, demonstrating the promise of two electrode materials for asymmetric device applications.

3.1 Characteristics of MCNF free-standing cathode

Figure 2 shows various physicochemical properties of MXene, CNF, and MCNF electrode. As shown in Fig. 2(a), TEM revealed the morphology of the as-prepared MXene nanosheets, transparent flakes with an average lateral dimension of several hundred nanometers. The inset in Fig. 2(a) shows an obvious Tyndall effect of MXene colloidal solution, it is a consequence of the abundance of oxygen-containing groups on the surface. Figure 2(b) shows the HR-TEM image of MXene, where the lattice fringes can be clearly observed and the measured interplanar spacing is 0.26 nm. The selected area electron diffraction (SAED) image (Fig. 2(c)) exhibits a symmetric hexagonal shape, which is consistent with the results of other studies [44]. The TEM image of CNF (Fig. 2(d)) shows that the average fiber size is about 5 nm in diameter and about 1 μm in length, showing an extremely high aspect ratio. The inset in Fig. 2(d) also shows the apparent Tyndall

effect of the CNF colloidal solution, which is a consequence of the abundance of hydroxyl functional groups on the CNF surface.

The physicochemical properties and morphological structures of the membranes with different CNF contents of MCNF obtained by simple vacuum filtration method were also characterized. FE-SEM was used to observe the surface and cross-section morphologies of the prepared films. Figures 2(e)–2(h) show the cross-sections of the hybrid films with different CNF percentages, respectively. It directly reveals the gradually widened interlayer gap in the increasingly loose film, resulting in an increased thickness from 6 μm for pure MXene film to 13 μm for the MCNF-16 hybridfilm. The lamellar structure of the composite membrane did not change significantly compared with pristine MXene membrane, and the surface of the self-supported membrane remained smooth even though the CNF loading was increased to 16%.

Figure 3(a) shows the layer structure bonding state of MXene film on the surface and part of the profile. While Fig. 3(b) reveals that the pristine MXene film exhibits a clear diffraction peak associated with the MXene basal plane. The peak shifts from 5.84° (*d*-spacing of 15.1 Å) to 5.6° (*d*-spacing of 15.8 Å) when the CNF loading is increased from 0% to 16%. This demonstrates that the CNF addition is effectively incorporated into the interlayer of the MXene sheet to increase the layer spacing, which agrees well with the FE-SEM data. As shown in Fig. 1(a), CNF acts as the connecting agent link in the hybrid film due to its large aspect ratio and high strength, and it is tightly bonded with the 2D MXene nanosheets through hydrogen bonding to significantly increase the mechanical strength of the composite film.

The elemental composition and chemical bonding states of all the prepared pure MXene films and MCNF hybrid films were analyzed by FTIR spectroscopy and XPS. It is clear that the symmetric stretching vibration peak of the –OH functional group in the FTIR spectra of Fig. 3(c) shifted from 3434 cm^{-1} (MXene film) to 3425 cm^{-1} (MCNF hybrid film). The stretching vibration peak of the C=O functional group shifted from 1632 cm^{-1} (MXene film) to 1628 cm^{-1} (MCNF hybrid film), confirming that the hydrogen bond between CNF and MXene brings the two phases closely. In addition, the XRD was used to test the structural
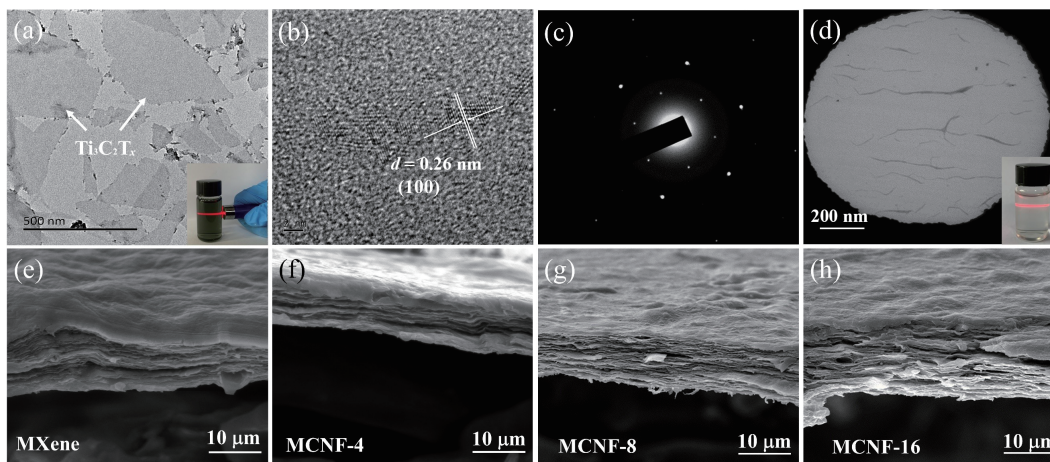
Figure 2 (a) TEM image of delaminated MXene nanosheets. The inset in (a) shows a photo of the colloidal suspension containing few-layered $Ti_3C_2T_x$ MXene flake and Tyndall effect, (b) HRTEM image of $Ti_3C_2T_x$ MXene, (c) SAED pattern of MXene nanoparticles, (d) TEM image of CNF, and (e)–(h) cross-section SEM images of pure MXene, MCNF-4, MCNF-8, and MCNF-16 films.
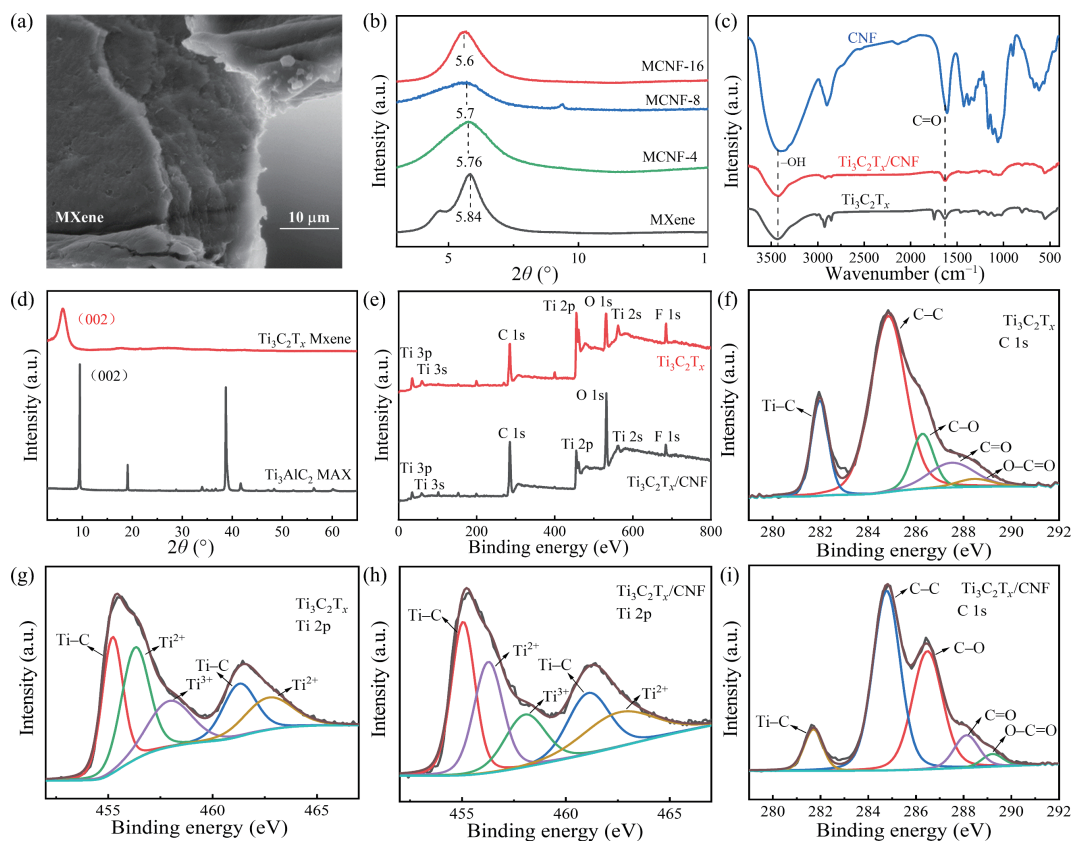

Figure 3 (a) Top view image of MXene film. (b) XRD patterns of MCNF film with different contents of CNF. (c) FTIR spectra of MXene, CNF, and MCNF. (d) XRD patterns of the MAX precursor and delaminated MXene. (e) XPS spectra of MCNF and MXene. High-resolution XPS spectra of (f) C 1s and (g) Ti 2p of pure MXene; high-resolution XPS spectra of (h) Ti 2p and (i) C 1s of MCNF composites.

characteristics of the MAX phase before and after etching. Figure 3(d) depicts that the MAX peak at 38.7° disappeared obviously, indicating that the intermediate aluminum atomic layer was successfully selectively etched away. The (002) characteristic peak shift from 9.5° to 6.1° is a typical feature of MXene with interlayer water molecules, indicating an increase in the interlayer spacing.

The XPS spectra (Fig. 3(e)) illustrate that both MXene film and MCNF film contain the element of C, O, F, and Ti. Compared with pure MXene membrane, the atomic percentages of C and O elements increased and those of Ti and F elements decreased in the MCNF hybrid membrane. This is presumably ascribed to the fact that the added CNF increased the contents of C and O elements. No new peaks appeared in the deconvoluted Ti 2p spectrum (Figs. 3(g) and 3(h)) of MCNF hybrid membranes

compared with pure MXene membranes, indicating that the addition of CNF did not change the chemical bonding state of MXene itself. For the high-resolution C 1s spectra (Figs. 3(f) and 3(i)) of MXene and MCNF, the binding energies of C–O and C=O functional groups increased from 286.2 and 287.5 to 286.5 and 288.1 eV, respectively, which are caused by the binding between the hydroxyl group of the CNF and the abundant oxygen-containing functional groups on the surface of MXene. The increase in the proportion of C–O groups and the decrease of Ti–C groups also provide evidence of the formation of hydrogen bonds, while the change in bond energy in Ti 2p is also attributed to this [45]. The observations of FTIR and XPS are consistent well with the previous studies [46, 47]. These result from the formation of strong hydrogen bonds between the abundant hydroxyl groups

on the surface of nanocellulose and the surface groups of MXene.

Additionally, the MCNF paper can be easily fabricated by the vacuum-assisted filtration process (with a diameter of 4 cm as displayed in Figs. 4(a), and Fig. 4(b) also exhibits the flexibility of the hybrid film) and maintains the excellent flexibility and foldability. As shown in Figs. 4(c) and 4(d), the tensile strength of the composite film is as high as 30.6 MPa when CNF content is at 16%, which is 5.6 times higher than that of the pristine MXene film (5.5 MPa) and Young's modulus is also increased from 2.3 to 3.2 MPa. The results of XPS, XRD, and FTIR spectra also demonstrate that the strong interfacial interaction between CNF and MXene phases is mainly generated by the hydrogen bonding formed by the van der Waals interactions between the numerous hydroxyl groups on the surface of CNF and the oxygen-containing groups on the surface of MXene. The nacre-inspired structure consisting of CNF with large aspect ratio and ultra-thin MXene sheets is also responsible for the enhanced stability of the mechanical strength [23, 30].

3.2 Electrochemical performances of MCNF free-standing cathode

To evaluate the electrochemical properties of the hybrid films and elucidate the effect of CNF on the hybrid membrane electrodes, the electrochemical performances of MXene, MCNF-4, MCNF-8, and MCNF-16 film electrodes were investigated in a three-electrode configuration in 1 M H_2SO_4. The CV curves of MXene and different MCNF membrane electrodes are shown in Figs. 5(a) and 6(a)–6(d). The gravimetric capacitances of MXene, MCNF-4, MCNF-8, and MCNF-16 at a scan rate of 5 mV·s^{-1} were calculated from the CV curves (Fig. 5(a)) as 251, 246, 242, and 212 F·g^{-1}, respectively, indicating that the presence of a limited amount of CNF does not gravely lower the capacitance of the hybrid membrane. All CV curves in the operating potential window of −0.7 to 0.2 V (versus Ag/AgCl) exhibit a pair of obvious redox peaks, indicating that the addition of CNF did not alter the pristine pseudocapacitance-involved charge storage mechanism of MXene, but the shift of peak position might be triggered by the change of functional groups on the surface of MXene (Figs.

6(a)–6(d)). As shown in Fig. 5(d) for the MCNF electrodes with different CNF loadings, the measured surface capacitance at 5 mV·s^{-1} is 452, 562, 491, and 256 mF·cm^{-2}, respectively. This proves that CNF provides an intercalation effect, which reduces the self-stacking of MXene flakes and provides more abundant reaction sites for ion transfer [33]. The non-conductivity of CNF is the fundamental factor that contributes to the electrochemically inactive and thus decreases the gravimetric capacitances of MCNF.

The electrochemical impedance spectra of different electrodes explain the capacitance variation in terms of resistance and electrochemical kinetics. In the high-frequency region, the real axis intercept corresponds to the equivalent series resistance (or internal resistance (R_s)), while the R_s values of 2.6, 5.3, 11.3, and 13.9 Ω in Fig. 5(c) correspond to pure MXene, MCNF-4, MCNF-8, and MCNF-16 electrodes, respectively. Furthermore, the semicircular diameters of MCNF-8 and MCNF-16 in the high-frequency region are significantly larger than those of MXene and MCNF-4, which is determined by the insulative nature of CNF, and the reason for the decrease in the gravimetric capacitances of the hybrid film is verified. In the low-frequency region, MCNF-4 and MCNF-8 exhibit a near vertical line similar to that of pure MXene, showing extinguished ionic diffusion and capacitive behavior. In contrast, the nearly 45° linear part of MCNF-16 indicates its slow ion diffusion ability, which explains the dramatic decrease in capacitive performance.

The MCNF-4 electrode exhibits good rate performance with a capacitance of 71 F·g^{-1} (162 mF·cm^{-2}) at a scan rate of 100 mV·s^{-1}, compared to 65 F·g^{-1} (136 mF·cm^{-2}) and 20 F·g^{-1} (24 mF·cm^{-2}) for the MCNF-8 and MCNF-16, respectively. GCD curves for each electrode are displayed in Figs. 5(b) and 6(e)–6(h). The charge/discharge curves of all electrodes at different current densities are triangle-like (characteristic of pseudocapacitive behavior) and display a good symmetry, demonstrating the extremely high coulomb efficiency of the electrodes (surface redox reaction is highly reversible) (Figs. 6(e)–6(h)).

The addition of 4% CNF to $Ti_3C_2T_x$ decreased the gravimetric capacitance (about 2%) but the mechanical strength of MCNF-4
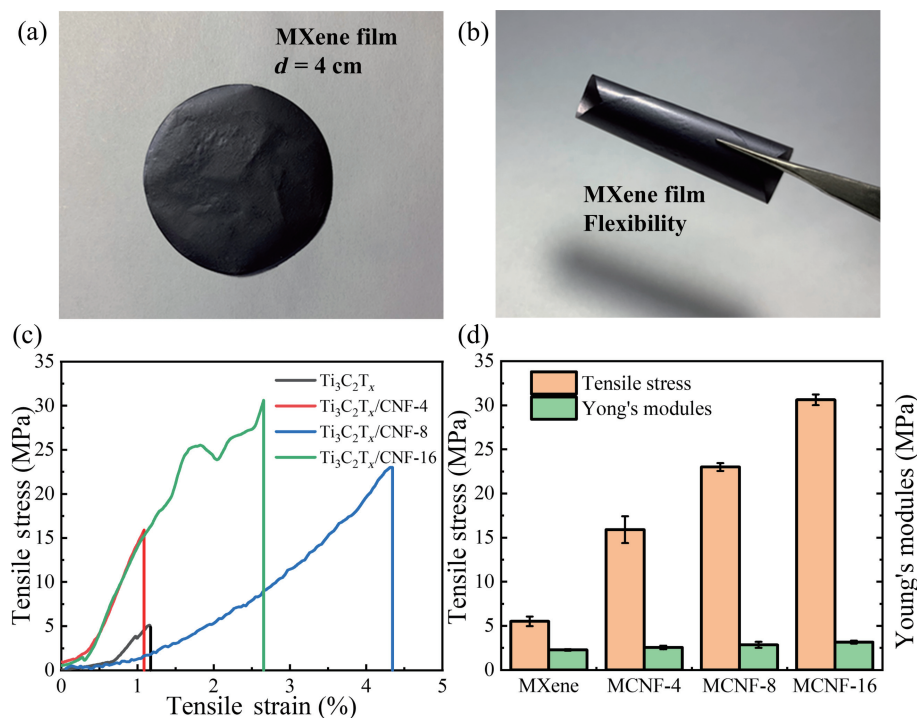

Figure 4 (a) An optical image of MCNF film, (b) optical image of MCNF film and flexibility exhibition, (c) tensile stress–strain curves of composites films, and (d) tensile strength and Young's modules of MCNF and pure MXene nanopapers.
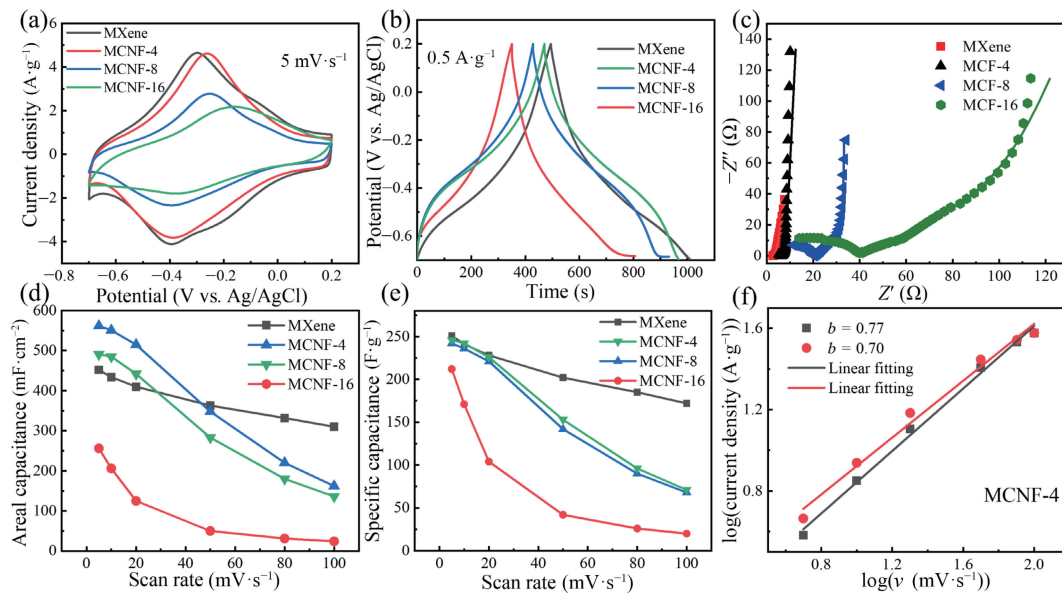
Figure 5 Electrochemical performance of MCNF electrode in 1 M H$_2$SO$_4$ in a three-electrode configuration. (a) CV curves of MCNF-X and MXene at scan rates of 5 mV·s^{-1}, (b) GCD curves of MCNF-X and MXene at current density of 0.5 A·g^{-1}, (c) Nyquist plots of MCNF-X and MXene, the solid line represents the corresponding equivalent circuit fitting result, (d) areal capacitances of MCNF-X and MXene at different scan rates, (e) gravimetric capacitances of MCNF-X and MXene at different scan rates, and (f) logarithm plot of cathodic and anodic peak currents as a function of scan rate.
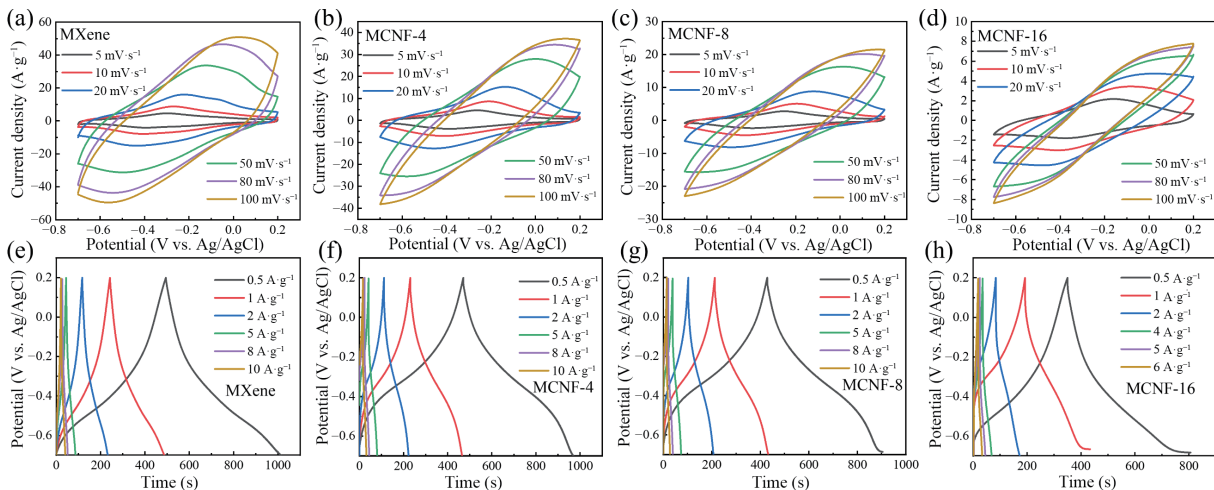

Figure 6 CV curves at different scan rates for (a) pristine MXene, and MCNF nanocomposite electrodes with (b) 4% CNF, (c) 8% CNF, and (d) 16% CNF in three-electrode system. Galvanostatic charge–discharge profiles at different current densities for (e) pristine MXene, and MCNF nanocomposite electrodes with (f) 4% CNF, (g) 8% CNF, and (h) 16% CNF in three-electrode system.

(15.9 MPa) was increased by 290% than that of the pristine MXene (5.5 MPa) electrode. When the CNF content was increased to 16%, the mechanical strength was increased up to 5.6 times of the original electrode (30.6 MPa), but there was also a severe loss of capacitance (about 16%). The increase in mechanical strength is more significant for MCNF-16 nanocomposite paper, which showed a higher mechanical strength (30.6 MPa) with 16% lower gravimetric capacitance. In order to strike a balance between high mechanical strength and high electrochemical performance, MCNF-4 electrodes were selected to continue the study of asymmetric capacitors.

The significantly increased mechanical strength of the ultrathin hybrid film electrode can compensate the slight sacrifice in capacitive performance, which is especially useful in applications where structural multifunctional electrodes are required. The charge storage mechanism of the MCNF-4 electrode can be explored by studying the power law relationship between the CV peak current (i) and the scan rate (v) following Eq. (8)

$$i = av^b \tag{8}$$

where a and b are adjustable parameters, mapping $\log(i)$ to $\log(v)$

will give a straight line and the slope of the line is b value. When $b = 1$, the charge storage kinetics is a surface-controlled capacitive process; and when $b = 0.5$, the charge storage kinetics is a diffusion-controlled process. As shown in **Fig. 5(f)**, the b-values of the anodic and cathodic peaks of the MCNF-4 electrode are 0.77 and 0.70, respectively, indicating that the dominant charge storage mechanism is surface redox reaction and double-layer contributions, which is consistent with the previously reported mechanism of pure MXene electrode and has not been changed by the addition of CNF [48].

3.3 Characteristics of CP flexible anode

Figures 7 and 8 show various physicochemical properties of CC/PANI electrode. Here, CC with high mechanical strength, excellent flexibility, and positive conductivity was selected as the anode substrate, and preparation process of CP electrode was conducted by a simple two-step method. Firstly, CC was completely impregnated in aniline monomer/HCl solution to ensure ANI penetrate into the internal structure, and then aniline was polymerized on each thread surface of CC to form nanostructured PANI particles. **Figures 7(a)** and **7(b)** show the
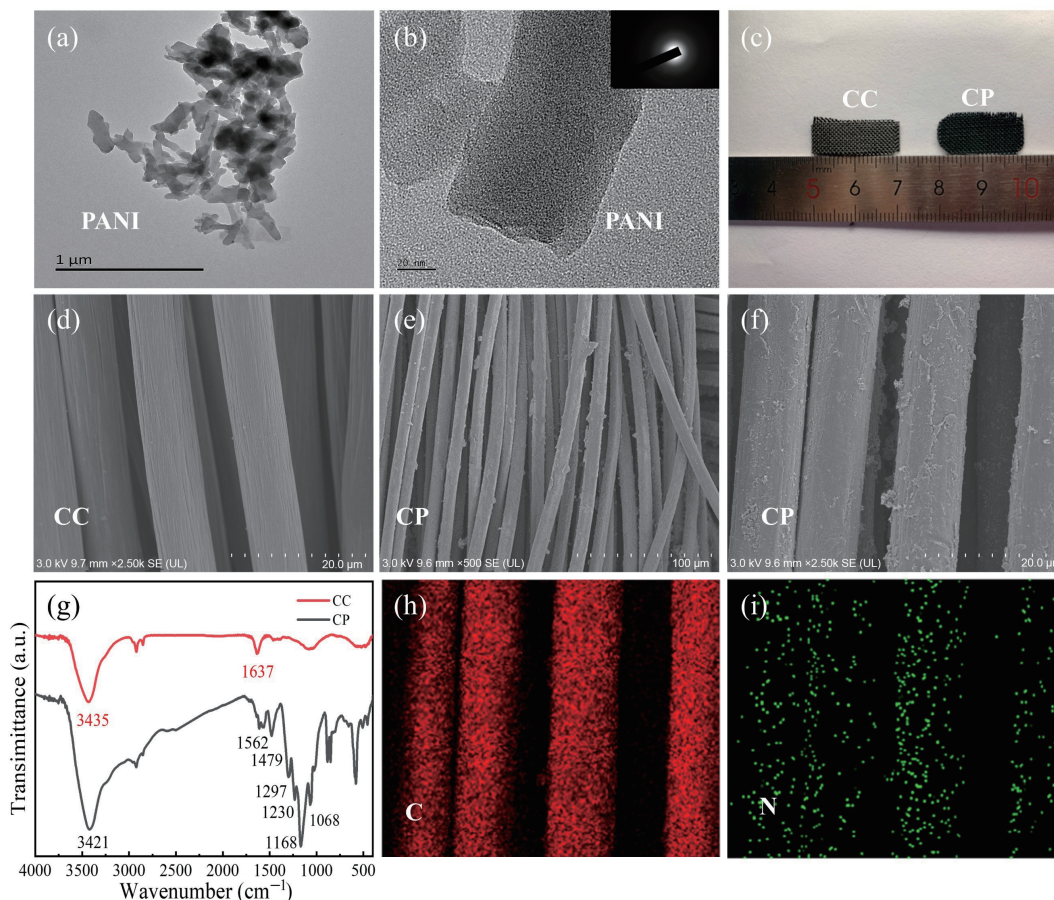
Figure 7 (a) TEM image of PANI nanoparticles, (b) the HRTEM image of PANI nanoparticles. The inset in (b) shows the SAED pattern of PANI nanoparticles, (c) digital images showing substrate before polymerization (CC, left) and substrate after polymerization (CP, right). FE-SEM images for (d) CC and (f) CP. (e) FE-SEM images for CP at low magnification, (g) FTIR spectra of CC and CP, FE-SEM images of CP electrode, (h) C mapping and (i) N mapping.
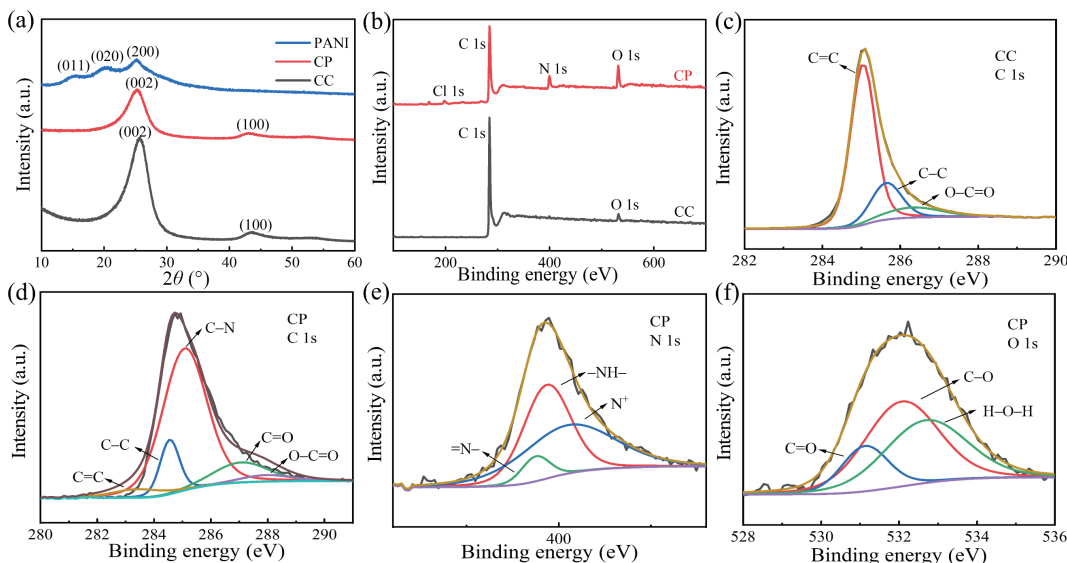

Figure 8 (a) XRD patterns of the CC, CP, and PANI, (b) XPS spectra of CC and CP, (c) high-resolution XPS spectra of C 1s of CC, and (d)–(f) high-resolution XPS spectra of C 1s, N 1s, and O 1s of CP.

TEM and HR-TEM images of PANI nanoparticles formed during the *in-situ* polymerization. As can be easily observed in Fig. 7(a), plenty of PANI nanoparticles aggregated together with a diameter of about 80 nm and a length of about 300 nm. Its HR-TEM image is shown in Fig. 7(b), which is typical of PANI fiber morphology, and the amorphous heterogeneous surface of the material is demonstrated by SAED pattern (inset of Fig. 7(b)). From the digital images of CC and CP (Figure. 7(c)), it can be observed that the color of the CC after polymerization changes from the original

gray to dark green, and the PANI was closely bonded to the substrate to withstand the wear and tear of characterization process.

The morphological structures of CC, CP, and PANI were observed by FE-SEM and TEM (including HR-TEM), respectively. Figures 7(d)–7(f) show the FE-SEM images of CC (before PANI polymerization) and CP (after polymerization), respectively. It is observed that the thread diameter of the unpolymerized CC is about 8 μm, with a smooth and flat surface,

and the gap between the fibers still retains about a few microns, which is conducive to the full contact between the aniline monomer and the fiber surface. In contrast, the thread diameter of the CP reached about 9 µm, and the roughness of the thread surface was modified (the larger specific surface area can provide additional redox reaction sites for the electrolyte ions), which can obtain a higher electrochemical performance. FE-SEM images show that PANI was evenly and densely wrapped around the CC to form a core–shell structure. The EDS mapping images (Figs. 7(h) and 7(i)) also illustrate that the N elements of PANI are uniformly distributed on the CC substrate.

Figure 7(g) exhibits the FTIR spectra of CC and CP. The wide peaks at 3435 and 3421 cm^{-1} are the stretching vibration peaks caused by the hydroxyl groups of CC and CP, respectively. The CP spectra of 1562 and 1479 cm^{-1} are related to the skeletal vibrations of the quinone and benzene rings, respectively, while 1297 and 1230 cm^{-1} are due to the N–B–N stretching vibrations and N=Q=N electronic-like absorption [49, 50]. Meanwhile, the bands at 1168 and 1068 cm^{-1} are ascribed to the aromatic C–H bending in the plane of the aromatic ring. The common characteristic band of PANI observed on the CP spectra indicates the successful polymerization of PANI on CC, which agrees with the results of FE-SEM, XPS, and XRD analysis.

The preparation of PANI electrodes by conventional methods may have the disadvantage of nanoparticle agglomeration due to the addition of binder and conductive agent. This severely diminishes the specific surface area and porosity of the active material and thus prevents the ions in the electrolyte from fully contacting the active substance and from rapidly accumulating and transferring ultimately damaging the electrochemical performance [51]. Therefore, rather than traditional electrode preparation method, the *in-situ* polymerization method was chosen to prepare electrodes.

The crystal structure of PANI was analyzed by XRD for any obvious changes before and after bonding with CC in Fig. 8(a). The XRD patterns of CC present two distinctive peaks at 25.7° and 43.6° from (002) and (100) planes reflections, respectively. The intensity of the diffraction peaks corresponding to CP at (002) and (100) is weakened compared to CC, indicating that the PANI particles are uniformly and continuously wrapped on the CC surface. CP exhibits a high degree of crystallinity and the peak at $2\theta = 25.3°$ is due to the periodicity perpendicular to the polymer chain. Moreover, no new diffraction peaks appear compared to PANI, but the peak intensities are significantly higher than PANI, presumably due to the skeletal effect of CC driving the orderly crystallization of the conducting polymer molecular chains [52]. The disappearance of the diffraction peaks (011) and (020) and the larger half-peak width of (002) may be explained by the covalent interaction between PANI and CC, resulting in a homogeneous distribution of PANI on the surface of the carbon fabric fibers and an increase in the d-spacing ($2\theta = 25.3°$) [53].

The elemental composition and chemical bonding states of CC and CP hybrid electrodes were analyzed by XPS. Figure 8(b) depicts the survey scan spectra of CC and CP. Compared with the CC spectrum, in addition to the existing C 1s peak (284.5 eV) and O 1s peak (532.5 eV), the N 1s (399.6 eV) peak and Cl 1s (197.6 eV) peak newly appear in the CP spectrum, indicating that PANI was successfully polymerized on CC. The appearance of the Cl peak is due to the use of HCl as an acidic medium and dopant in the polymerization process, which protonates the polymer chains thereby forming the higher conductivity emeraldine salt form of PANI [54, 55].

The deconvoluted spectrum of CC at C 1s contains three peaks of graphitic carbon (285.1 eV), hydroxyl (285.6 eV), and carboxyl groups (286.4 eV) (Fig. 8(c)). The C 1s, N 1s, and O 1s peaks in the CP spectra were further deconvoluted to investigate the elemental composition and chemical bonding state between PANI and CC, respectively. The deconvolution spectrum of C 1s (Fig. 8(d)) with the peak at 285.1 eV corresponds to the C–N configurations, indicating the successful polymerization of PANI on the CC. The other peaks in the C 1s XPS spectrum of the CP at 283.4, 284.5, 287.1, and 288.0 eV are assigned to the C=C, C–C, C=O, and O–C=O groups, respectively. Compared to CC, a few peak positions in CP move towards lower binding energies, which may be caused by the superior electrical conductivity of the CP surface. The improved conductivity may counteract the accumulation of positive charges, which allows for the loss of photoelectrons during XPS measurements [56]. The N 1s peaks of CP in Fig. 8(e) are deconvoluted into three peaks associated with quinimine amine (=N–), benzimine amine (–NH–), and nitrogen cationic radical (N⁺), centered at 399.4, 399.7, and 400.4 eV, respectively [57, 58]. This part of the nitrogen, which has been successfully protonated (N⁺), facilitates the enhancement of the electrode conductivity [59]. The deconvoluted spectra of O 1s at 531.1, 532.1, and 532.7 eV correspond to the subpeaks of C=O, C–O and H–O–H, respectively, and the appearance of these peaks is presumably explained by the presence of bound water in PANI (Fig. 8(f)).

3.4 Electrochemical performance of CP flexible anode

Figure 9 depicts the electrochemical performance of CC and CP electrodes in the three-electrode test system with 1 M H_2SO_4 electrolyte and a voltage window of 0–0.8 V. Figure 9(a) shows the CV curves of the samples CC and CP at 5 mV·s^{-1}. It can be seen that the CV curve of CC behaves almost as a line for the negligibly low capacitance (0.3 F·g^{-1}, 2.9 mF·cm^{-2}). While the CP exhibits a pair of redox peaks at 0.1 and 0.3 V, the formation of which is mainly attributed to the leucoemeraldine–emeraldine redox transformation of PANI, the other pair of redox peaks located at 0.58 and 0.5 V high anodic potentials are due to the degradation of PANI and the emeraldine-pernigraniline transition [60, 61]. The redox peaks are distinctly visible in the CV curves of the CP electrode at all scan rates range from 5 to 100 mV·s^{-1}, which corresponds to the non-ideal triangular curve exhibited by the GCD curve, and this phenomenon belongs to the obvious pseudocapacitive behavior (Figs. 9(b) and 9(c)).

From the Nyquist plot of the CC and CP electrodes (Fig. 9(d)), the R_s of the CP in the high frequency region is 4.1 Ω, which is slightly smaller than the CC electrode (4.9 Ω), while both electrodes behave as nearly vertical lines in the low frequency region, providing a smooth channel for ion transport and thus exhibiting an ideal capacitive behavior. The main reasons for this situation are as follows: The two materials CC and PANI possess high electrical conductivity, and the core–shell structure of CP is a reasonable structural design for the combination of the two materials, which effectively ensures the specific surface area and more abundant reactive sites compared with the traditional preparation of electrodes, rendering the ion transfer more efficiently [51]. The capacitive contribution was further analyzed using Eq. (8), and the b values of anodic peak and cathodic peak obtained from Fig. 9(e) are 0.94 and 0.87, respectively, indicating that the current response is predominantly capacitive response. The specific capacitance of the CP electrode was 699 F·g^{-1} (350 mF·cm^{-2}) when the sweep rate was 5 mV·s^{-1}, and 521 F·g^{-1} (261 mF·cm^{-2}) when the scan rate was increased to 100 mV·s^{-1}, which indicates an excellent rate capability (Fig. 9(f)).

3.5 Electrochemical performance of the MCNF/CP asymmetric supercapacitors

Since the CP and MCNF electrodes demonstrated promising electrochemical performance in 1 M aqueous H_2SO_4 electrolyte, they were assembled as positive and negative electrodes,
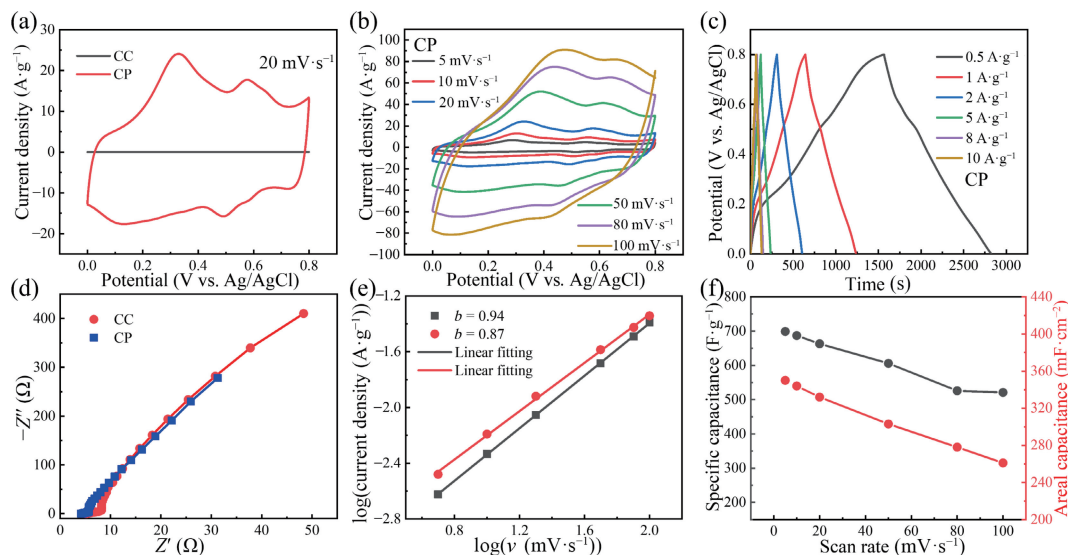
Figure 9 Electrochemical performance of CP and CC electrode in 1 M H₂SO₄ in a three electrodes configuration. (a) CV curves of CC and CP at constant scan rate of 20 mV·s⁻¹, (b) CV curves of the CP electrode at various scan rates, (c) galvanostatic charge–discharge profiles of CP electrode at different current densities, (d) Nyquist plots of CC and CP, the solid line represents the corresponding equivalent circuit fitting result, (e) the power-law dependence of peak current density at scan rates from 5 to 100 mV·s⁻¹, and (f) gravimetric capacitances and areal capacitances of CP electrode at different scan rates.

respectively, to form a solid-state flexible asymmetric supercapacitor. As shown in Fig. 10(a), the potential operating windows of the MCNF and CP electrodes are −0.7–0.2 and 0–0.8 V, respectively, so the theoretical maximum operating voltage of the assembled ASC can reach 1.5 V. Balancing the charge between the cathode and anode ($q^+ = q^-$) by adjusting the mass of active material in MCNF and CP electrode (M_{MCNF}:$M_{CP} \approx 2.5{:}1$) is an inevitable step prior to the assemble of asymmetric devices, which facilitates the maximization of device capacitance.

Figure 10(b) shows the CV curves of the as-prepared ASC with the operating voltage window from 0.9 to 1.7 V at a scan rate of 20 mV·s⁻¹. The CV curve shape remains good when the closed-circuit voltage increases from 0.9 to 1.5 V, indicating a good capacitive behavior within 0–1.5 V. While as the cutoff voltage is further increased to 1.7 V, it causes a severe polarization due to the decomposition of water. At a scan rate of 5 mV·s⁻¹, the CV curve of ASC exhibits a pair of distinct broad redox peaks, indicating that the redox pseudocapacitance contributes to the primary capacitance of the device. This phenomenon can also be evidenced by the fact that the GCD profiles of the ASC exhibit a period of bulge in the potential window at 0.4–1.0 V (Figs. 10(c) and 10(d)). The superior conductivity and rapid charge transfer kinetics of the MCNF anode and CP cathode are the radical reasons why the cyclic voltametric curves of ASC maintain undistorted at a high scan rate of 100 mV·s⁻¹. As depicted in Fig. 10(e), the specific capacitance of ASC is 97 F·g⁻¹ (281 mF·cm⁻²) at the scan rate of 5 mV·s⁻¹; the specific capacitance of 41 F·g⁻¹ (113 mF·cm⁻²) is still maintained when the scan rate is increased to 100 mV·s⁻¹, which indicates a good rate capability.

The Nyquist plot of the ASC is shown in Fig. 10(f), the nearly vertical lines in the low frequency region indicate the good ion diffusion capability of the device, and the small semicircle in the medium-frequency region indicates a lower charge transfer resistance. The R_s and charge transfer resistance (R_{ct}) obtained from the electric equivalent circuit of the inset are 2.7 and 15.0 Ω, respectively, indicating that the ASCs possess an extraordinary conductivity and electron transfer capability.

To investigate the charge storage kinetic mechanism of ASCs, the b values of 0.58 and 0.88 for the anodic and cathodic peaks, respectively, calculated with Eq. (8), indicate that the surface redox reaction is the major contribution to the capacitance (Fig. 10(g)). The ratio of capacitance contribution at different scan rates was

calculated according to Eq. (9)

$$i = k_1 v + k_2 v^{1/2} \tag{9}$$

where $k_1 v$ and $k_2 v^{1/2}$ correspond to the fraction of capacitive contribution and diffusion contribution, respectively [62]. Figure 10(h) indicates that the shaded area denotes a capacitance contribution of about 42% for a scan rate of 5 mV·s⁻¹, while the capacitance contribution rises to 81% for a scan rate of 100 mV·s⁻¹ (Fig. 10(i)). The fundamental explanation for the high percentage of capacitive contribution in charge storage is analyzed as follows. Firstly, the positive and negative electrode materials (CP and MCNF) both have a good electron conductivity, and then the microstructures of both electrodes are designed to facilitate the penetration of hydrogen ions into the surface structure of the active material [63].

The structure of this solid-state flexible asymmetric supercapacitor can be seen in Fig. 11(a). In the bending tests at different angles (0°, 45°, 90°, and 180°), as shown in Fig. 11(b), the almost overlapping CV curves of ASC prove the excellent flexibility and stability of the device. The device exhibits good cycling stability with a capacity retention rate of 86% of the initial capacitance after 5000 consecutive cycles of charge/discharge testing at high current density of 20A·g⁻¹ (Fig. 11(c)). The Ragone plots reflect the energy density and power density of ASC. MCNF//CP ASCs exhibit a remarkable electrochemical performance with a gravimetric energy density of 30.6 Wh·kg⁻¹ at a power density of 1211 W·kg⁻¹ and gravimetric energy density of 12.8 Wh·kg⁻¹ at a power density of 8023 W·kg⁻¹, indicating superior rate capability (Fig. 11(d)). The obtained energy density of MCNF//CP ASC exceeds that of many previously reported MXene or PANI-based supercapacitors (Table 1), including Ti₃C₂/CuS// Ti₃C₂ (1.5 V; 15.4 Wh·kg⁻¹) [64], Ti₃C₂/CC//RuO₂/CC (1.5 V; 29 Wh·kg⁻¹) [65], Ti₃C₂//PANI/rGO (1.45 V; 17 Wh·kg⁻¹) [66], V₂C/PANI//AC (1.5 V; 11.25 Wh·kg⁻¹) [67], Ti₃C₂//Phenothiazine/rGO (1.4 V; 17.4 Wh·kg⁻¹) [68], and Ti₃C₂//rGOH (1.1 V; 8Wh·kg⁻¹) [69]. In summary, this remarkable electrochemical performance, mechanical durability of the MCNF//CP ASC device demonstrates a possibility that it can serve as a reliable and powerful energy storage device for many potential and emerging applications.
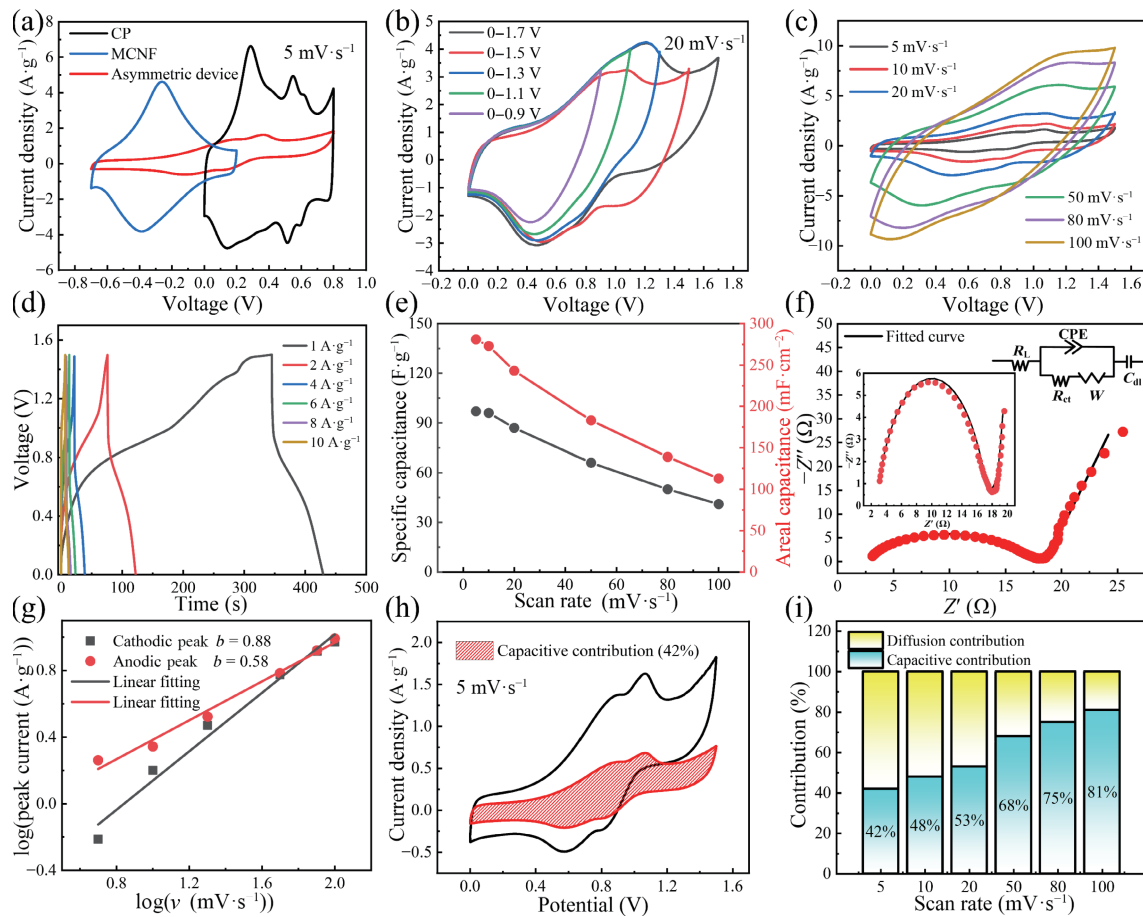
Figure 10 (a) CV curves of MCNF-4, CP, and the assembled asymmetric device at a scan rate of 5 mV·s⁻¹, (b) CV curves of the as-prepared device measured over the operating voltage windows from 0.9 to 1.7 V at a constant scan rate of 20 mV·s⁻¹, (c) CV curves collected at different scan rates between 0 and 1.5 V, (d) GCD curves measured at different current densities between 0 and 1.5 V, (e) areal capacitance and gravimetric capacitance based on the ASCs at scan rates varying from 5 to 100 mV·s⁻¹, (f) Nyquist plot of the ASC. Inset shows the electrical equivalent circuit model for the Nyquist plot. (g) Logarithm plot of cathodic and anodic peak currents as a function of scan rate, (h) CV curves at 5 mV·s⁻¹ with the shadowed area representing the surface capacitive contribution, and (i) percentage capacitive contributions obtained at a scan rate of 5, 10, 20, 50, 80, and 100 mV·s⁻¹.
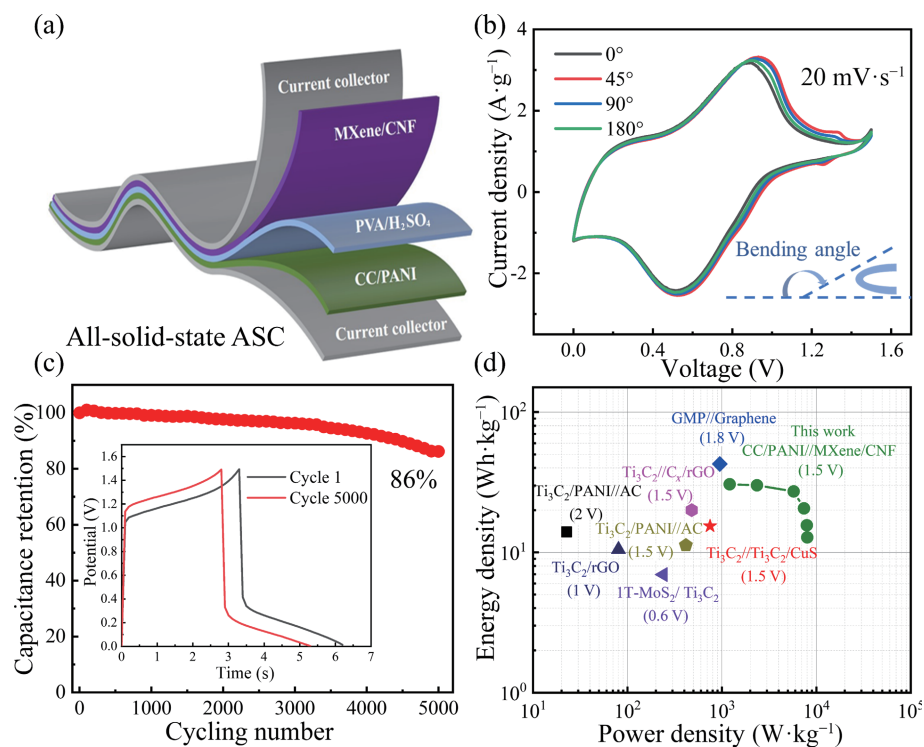

Figure 11 (a) Illustration of components of the MCNF//CP device, (b) CV curves of the asymmetric supercapacitor device under different bending states tested at 20 mV·s⁻¹, (c) cycling performance of the asymmetric supercapacitor device measured at 20 A·g⁻¹ and inset is the GCD profile at first cycle and after 5000 cycles, and (d) Ragone plots of solid-state MCNF//CP asymmetric supercapacitor in comparison to other state-of-the-art MXene-based and PANI-based supercapacitors.

Table 1 Comparison of the electrochemical performance of MXene-based supercapacitors

Electrode	Configuration	Electrolyte	Voltage (V)	Energy density (Wh·kg⁻¹)	kPower density (W·kg⁻¹)	References
Ti_3C_2/CNF//PANI/CC	Asymmetric	1 M H_2SO_4	1.5	30.6	1211	This work
Ti_3C_2/CuS// Ti_3C_2	Asymmetric	1 M KOH	1.5	15.4	750.2	[64]
Ti_3C_2//rGOH	Asymmetric	1 M H_2SO_4	1.1	8	NA	[69]
Ti_3C_2/rGO	Symmetric	3 M H_2SO_4	1	10.5	80.3	[70]
Ti_3C_2/CC// RuO_2/CC	Asymmetric	1 M H_2SO_4	1.5	29	3800	[65]
1T-MoS_2/ Ti_3C_2	Symmetric	1 M H_2SO_4	0.6	6.95	239.48	[71]
N,O co-doped C@ Ti_3C_2	Symmetric	6 M KOH	1.2	10.8	600	[72]
Ti_3C_2/PANI//AC	Asymmetric	7 M KOH	2	22.67	14	[37]
Ti_3C_2// PANI/ rGO	Asymmetric	3 M H_2SO_4	1.45	17	NA	[66]
Ti_3C_2/MnO_2/CC//AC	Asymmetric	3 M KOH	1.5	29.58	749.92	[73]
Ti_3C_2//Cx/ rGO	Asymmetric	3 M H_2SO_4	1.5	20	480	[74]
Ti_3C_2//Phenothiazine/rGO	Asymmetric	3 M H_2SO_4	1.4	17.4	NA	[68]
V_2C/PANI//AC	Asymmetric	1 M H_2SO_4	1.5	11.25	415.38	[67]
A- Ti_3C_2/PANI	Symmetric	1 M H_2SO_4	1	20.3	500	[75]
Ti_3C_2/PANI-NTs	Symmetric	1 M H_2SO_4	0.8	25.6	153.2	[76]

4 Conclusions

All-pseudocapacitance MCNF//CP ASCs are designed with MCNF as the negative electrode and CP as the positive electrode. The charge storage mechanism of both positive and negative electrodes is contributed by the highly reversible protonation/deprotonation pseudocapacitance of surface functional groups, which can ensure good conductivity and high capacitance. By utilizing the complementary positive and negative potential windows, the assembled devices exhibit a wide voltage window of 1.5 V and a high gravimetric energy density of 30.6 Wh·kg⁻¹ and power density of 1211 W·kg⁻¹ in PVA/H_2SO_4 gel electrolyte. Moreover, the asymmetric device is still able to maintain a high capacitance retention of 86% at a high current density of 20 A·g⁻¹, demonstrating excellent electrochemical stability. Furthermore, due to the excellent flexibility of both positive and negative electrode materials, the bendability of the asymmetric device is also rather outstanding and no significant degradation of the capacitance performance is found in the bending test. This study provides a feasible guide to achieve the design and matched assembly of high-performance electrode structures for wide voltage window and high energy density pseudocapacitive ASCs. It is worth noting that the simple fabrication approach of positive and negative electrode materials and the convenient assembly of asymmetric devices enable the application of this flexible energy storage device in the field of flexible wearable electronic devices with tremendous potentials.

Acknowledgements

References

[1] Ma, Y. P.; Xie, X. B.; Yang, W. Y.; Yu, Z. P.; Sun, X. Q.; Zhang, Y. P.; Yang, X. Y.; Kimura, H.; Hou, C. X.; Guo, Z. H. et al. Recent advances in transition metal oxides with different dimensions as electrodes for high-performance supercapacitors. *Adv. Compos. Hybrid. Mater.* **2021**, *4*, 906–924.

[2] Gogotsi, Y.; Simon, P. True performance metrics in electrochemical energy storage. *Science* **2011**, *334*, 917–918.

[3] Wang, Y. G.; Song, Y. F.; Xia, Y. Y. Electrochemical capacitors: Mechanism, materials, systems, characterization and applications. *Chem. Soc. Rev.* **2016**, *45*, 5925–5950.

[4] Lu, X. H.; Yu, M. H.; Wang, G. M.; Tong, Y. X.; Li, Y. Flexible solid-state supercapacitors: Design, fabrication and applications. *Energy Environ. Sci.* **2014**, *7*, 2160–2181.

[5] Yi, F.; Ren, H. Y.; Shan, J. Y.; Sun, X.; Wei, D.; Liu, Z. F. Wearable energy sources based on 2D materials. *Chem. Soc. Rev.* **2018**, *47*, 3152–3188.

[6] Chen, C. J.; Zhang, Y.; Li, Y. J.; Dai, J. Q.; Song, J. W.; Yao, Y. G.; Gong, Y. H.; Kierzewski, I.; Xie, J.; Hu, L. B. All-wood, low tortuosity, aqueous, biodegradable supercapacitors with ultra-high capacitance. *Energy Environ. Sci.* **2017**, *10*, 538–545.

[7] Wang, R. H.; Xu, C. H.; Lee, J. M. High performance asymmetric supercapacitors: New NiOOH nanosheet/graphene hydrogels and pure graphene hydrogels. *Nano Energy* **2016**, *19*, 210–221.

[8] Dang, C. C.; Mu, Q.; Xie, X. B.; Sun, X. Q.; Yang, X. Y.; Zhang, Y. P.; Maganti, S.; Huang, M. N.; Jiang, Q. L.; Seok, I. et al. Recent progress in cathode catalyst for nonaqueous lithium oxygen batteries: A review. *Adv. Compos. Hybrid. Mater.* **2022**, *5*, 606–626.

[9] Yuan, H.; Wang, G.; Zhao, Y. X.; Liu, Y.; Wu, Y.; Zhang, Y. G. A stretchable, asymmetric, coaxial fiber-shaped supercapacitor for wearable electronics. *Nano Res.* **2020**, *13*, 1686–1692.

[10] Qi, G. Y.; Liu, Y.; Chen, L. L.; Xie, P. T.; Pan, D.; Shi, Z. C.; Quan, B.; Zhong, Y. M.; Liu, C. Z.; Fan, R. H. et al. Lightweight Fe₃C@Fe/C nanocomposites derived from wasted cornstalks with high-efficiency microwave absorption and ultrathin thickness. *Adv. Compos. Hybrid. Mater.* **2021**, *4*, 1226–1238.

[11] Tie, D.; Huang, S. F.; Wang, J.; Ma, J. M.; Zhang, J. J.; Zhao, Y. F. Hybrid energy storage devices: Advanced electrode materials and matching principles. *Energy Storage Mater.* **2019**, *21*, 22–40.

[12] Chen, L. F.; Huang, Z. H.; Liang, H. W.; Guan, Q. F.; Yu, S. H. Bacterial-cellulose-derived carbon nanofiber@MnO₂ and nitrogen-doped carbon nanofiber electrode materials: An asymmetric supercapacitor with high energy and power density. *Adv. Mater.* **2013**, *25*, 4746–4752.

[13] Choudhary, N.; Li, C.; Moore, J.; Nagaiah, N.; Zhai, L.; Jung, Y.; Thomas, J. Asymmetric supercapacitor electrodes and devices. *Adv. Mater.* **2017**, *29*, 1605336.

[14] Hou, C. X.; Yang, W. Y.; Kimura, H.; Xie, X. B.; Zhang, X. Y.; Sun, X. Q.; Yu, Z. P.; Yang, X. Y.; Zhang, Y. P.; Wang, B. et al. Boosted lithium storage performance by local build-in electric field derived by oxygen vacancies in 3D holey N-doped carbon structure decorated with molybdenum dioxide. *J. Mater. Sci. Technol.* **2023**, *142*, 185–195.

[15] Ahmed, F. B. M.; Khalafallah, D.; Zhi, M. J.; Hong, Z. L. Porous nanoframes of sulfurized NiAl layered double hydroxides and ternary bismuth cerium sulfide for supercapacitor electrodes. *Adv. Compos. Hybrid. Mater.* **2022**, *5*, 2500–2514.

[16] Zhang, Y. L.; Ma, Z. L.; Ruan, K. P.; Gu, J. W. Multifunctional Ti₃C₂Tₓ-(Fe₃O₄/polyimide) composite films with Janus structure for outstanding electromagnetic interference shielding and superior visual thermal management. *Nano Res.* **2022**, *15*, 5601–5609.

[17] Zhang, J. Z.; Seyedin, S.; Gu, Z. J.; Yang, W. R.; Wang, X. G.; Razal, J. M. MXene: A potential candidate for yarn supercapacitors. *Nanoscale* **2017**, *9*, 18604–18608.

[18] Hantanasirisakul, K.; Gogotsi, Y. Electronic and optical properties of 2D transition metal carbides and nitrides (MXenes). *Adv. Mater.* **2018**, *30*, 1804779.

[19] Shekhirev, M.; Shuck, C. E.; Sarycheva, A.; Gogotsi, Y. Characterization of MXenes at every step, from their precursors to single flakes and assembled films. *Prog. Mater. Sci.* **2021**, *120*, 100757.

[20] Zhang, Y. L.; Ruan, K. P.; Zhou, K.; Gu, J. W. Controlled distributed Ti₃C₂Tₓ hollow microspheres on thermally conductive polyimide composite films for excellent electromagnetic interference shielding. *Adv. Mater.*, in press, https://doi.org/10.1002/adma.202211642.

[21] Lukatskaya, M. R.; Mashtalir, O.; Ren, C. E.; Dall'Agnese, Y.; Rozier, P.; Taberna, P. L.; Naguib, M.; Simon, P.; Barsoum, M. W.; Gogotsi, Y. Cation intercalation and high volumetric capacitance of two-dimensional titanium carbide. *Science* **2013**, *341*, 1502–1505.

[22] Shao, L.; Xu, J. J.; Ma, J. Z.; Zhai, B. Y.; Li, Y.; Xu, R.; Ma, Z. L.; Zhang, G. H.; Wang, C. Y.; Qiu, J. H. MXene/RGO composite aerogels with light and high-strength for supercapacitor electrode materials. *Compos. Commun.* **2020**, *19*, 108–113.

[23] Cao, W. T.; Chen, F. F.; Zhu, Y. J.; Zhang, Y. G.; Jiang, Y. Y.; Ma, M. G.; Chen, F. Binary strengthening and toughening of MXene/cellulose nanofiber composite paper with nacre-inspired structure and superior electromagnetic interference shielding properties. *Acs Nano* **2018**, *12*, 4583–4593.

[24] Shao, Y. M.; Zhu, Y.; Zheng, R.; Wang, P.; Zhao, Z. Z.; An, J. Highly sensitive and selective surface molecularly imprinted polymer electrochemical sensor prepared by Au and MXene modified glassy carbon electrode for efficient detection of tetrabromobisphenol A in water. *Adv. Compos. Hybrid Mater.* **2022**, *5*, 3104–3116.

[25] Xie, X. Q.; Zhao, M. Q.; Anasori, B.; Maleski, K.; Ren, C. E.; Li, J. W.; Byles, B. W.; Pomerantseva, E.; Wang, G. X.; Gogotsi, Y. Porous heterostructured MXene/carbon nanotube composite paper with high volumetric capacity for sodium-based energy storage devices. *Nano Energy* **2016**, *26*, 513–523.

[26] Du, Y. T.; Kan, X.; Yang, F.; Gan, L. Y.; Schwingenschlögl, U. MXene/graphene heterostructures as high-performance electrodes

for Li-ion batteries. *ACS Appl. Mater. Interfaces* **2018**, *10*, 32867–32873.

[27] Zhang, Y. Z.; Cao, Z. J.; Liu, S. J.; Du, Z. G.; Cui, Y. L. S.; Gu, J. N.; Shi, Y. Z.; Li, B.; Yang, S. B. Charge-enriched strategy based on MXene-based polypyrrole layers toward dendrite-free zinc metal anodes. *Adv. Energy Mater.* **2022**, *12*, 2103979.

[28] Liang, Y.; Wei, Z.; Zhang, X. Y.; Wang R. G. Fabrication of vanadium oxide@polypyyrole (V₂O₅@PPy) core−shell nanofiber electrode for supercapacitor. *ES Energy Environ.* **2022**, *18*, 101–110.

[29] Li, B.; Guo, M. H.; Chen, X. Q.; Miao, Y. Y. Hydrothermally synthesized N and S co-doped mesoporous carbon microspheres from poplar powder for supercapacitors with enhanced performance. *Adv. Compos. Hybrid. Mater.* **2022**, *5*, 2306–2316.

[30] Chen, W. S.; Yu, H. P.; Lee, S. Y.; Wei, T.; Li, J.; Fan, Z. J. Nanocellulose: A promising nanomaterial for advanced electrochemical energy storage. *Chem. Soc. Rev.* **2018**, *47*, 2837–2872.

[31] Sun, Z.; Qi, H. J.; Chen, M. H.; Guo, S. T.; Huang, Z. H.; Maganti, S.; Murugadoss, V.; Huang, M. N.; Guo, Z. H. Progress in cellulose/carbon nanotube composite flexible electrodes for supercapacitors. *Eng. Sci.* **2022**, *18*, 59–74.

[32] Tian, W. Q.; VahidMohammadi, A.; Reid, M. S.; Wang, Z.; Ouyang, L. Q.; Erlandsson, J.; Pettersson, T.; Wågberg, L.; Beidaghi, M.; Hamedi, M. M. Multifunctional nanocomposites with high strength and capacitance using 2D MXene and 1D nanocellulose. *Adv. Mater.* **2019**, *31*, 1902977.

[33] Yang, W. Y.; Peng, D. N.; Kimura, H.; Zhang, X. Y.; Sun, X. Q.; Pashameah, R. A.; Alzahrani, E.; Wang, B.; Guo, Z. H.; Du, W. et al. Honeycomb-like nitrogen-doped porous carbon decorated with Co₃O₄ nanoparticles for superior electrochemical performance pseudo-capacitive lithium storage and supercapacitors. *Adv. Compos. Hybrid. Mater.* **2022**, *5*, 3146–3157.

[34] Hu, M. M.; Cui, C.; Shi, C.; Wu, Z. S.; Yang, J. X.; Cheng, R. F.; Guang, T. J.; Wang, H. L.; Lu, H. X.; Wang, X. H. High-energy-density hydrogen-ion-rocking-chair hybrid supercapacitors based on Ti₃C₂Tₓ MXene and carbon nanotubes mediated by redox active molecule. *ACS Nano* **2019**, *13*, 6899–6905.

[35] Feng, J. X.; Ding, L. X.; Ye, S. H.; He, X. J.; Xu, H.; Tong, Y. X.; Li, G. R. Co(OH)₂@PANI hybrid nanosheets with 3D networks as high-performance electrocatalysts for hydrogen evolution reaction. *Adv. Mater.* **2015**, *27*, 7051–7057.

[36] Miao, F. J.; Shao, C. L.; Li, X. H.; Wang, K. X.; Lu, N.; Liu, Y. C. Electrospun carbon nanofibers/carbon nanotubes/polyaniline ternary composites with enhanced electrochemical performance for flexible solid-state supercapacitors. *ACS Sustainable Chem. Eng.* **2016**, *4*, 1689–1696.

[37] Li, Y.; Kamdem, P.; Jin, X. J. Hierarchical architecture of MXene/PANI hybrid electrode for advanced asymmetric supercapacitors. *J. Alloys Compd.* **2021**, *850*, 156608.

[38] Ahirrao, D. J.; Mohanapriya, K.; Wilson, H. M.; Jha, N. Solar reduced porous graphene incorporated within polyaniline network for high-performance supercapacitor electrode. *Appl. Surf. Sci.* **2020**, *510*, 145485.

[39] Zhou, J. H.; Kang, Q.; Xu, S. C.; Li, X. G.; Liu, C.; Ni, L.; Chen, N. N.; Lu, C. L.; Wang, X. Z.; Peng, L. M. et al. Ultrahigh rate capability of 1D/2D polyaniline/titanium carbide (MXene) nanohybrid for advanced asymmetric supercapacitors. *Nano Res.* **2022**, *15*, 285–295.

[40] Shang, T. X.; Lin, Z. F.; Qi, C. S.; Liu, X. C.; Li, P.; Tao, Y.; Wu, Z. T.; Li, D. W.; Simon, P.; Yang, Q. H. 3D macroscopic architectures from self-assembled MXene hydrogels. *Adv. Funct. Mater.* **2019**, *29*, 1903960.

[41] Ko, Y.; Kwon, M.; Bae, W. K.; Lee, B.; Lee, S. W.; Cho, J. Flexible supercapacitor electrodes based on real metal-like cellulose papers. *Nat. Commun.* **2017**, *8*, 536.

[42] Lu, X. J.; Dou, H.; Yang, S. D.; Hao, L.; Zhang, L. J.; Shen, L. F.; Zhang, F.; Zhang, X. G. Fabrication and electrochemical capacitance of hierarchical graphene/polyaniline/carbon nanotube ternary composite film. *Electrochim. Acta* **2011**, *56*, 9224–9232.

[43] Ahirrao, D. J.; Pal, A. K.; Singh, V.; Jha, N. Nanostructured porous polyaniline (PANI) coated carbon cloth (CC) as electrodes for

flexible supercapacitor device. *J. Mater. Sci. Technol.* **2021**, *88*, 168–182.

[44] Zhou, G. Q.; Li, M. C.; Liu, C. Z.; Wu, Q. L.; Mei, C. T. 3D printed Ti$_3$C$_2$T$_x$ MXene/cellulose nanofiber architectures for solid-state supercapacitors: Ink rheology, 3D printability, and electrochemical performance. *Adv. Funct. Mater.* **2022**, *32*, 2109593.

[45] Wan, S. J.; Li, X.; Wang, Y. L.; Chen, Y.; Xie, X.; Yang, R.; Tomsia, A. P.; Jiang, L.; Cheng, Q. F. Strong sequentially bridged MXene sheets. *Proc. Natl. Acad. Sci. USA* **2020**, *117*, 27154–27161.

[46] Ma, Z. L.; Kang, S. L.; Ma, J. Z.; Shao, L.; Wei, A. J.; Liang, C. B.; Gu, J. W.; Yang, B.; Dong, D. D.; Wei, L. F. et al. High-performance and rapid-response electrical heaters based on ultraflexible, heat-resistant, and mechanically strong aramid nanofiber/Ag nanowire nanocomposite papers. *ACS Nano* **2019**, *13*, 7578–7590.

[47] Zhou, B.; Zhang, Z.; Li, Y. L.; Han, G. J.; Feng, Y. Z.; Wang, B.; Zhang, D. B.; Ma, J. M.; Liu, C. T. Flexible, robust, and multifunctional electromagnetic interference shielding film with alternating cellulose nanofiber and MXene layers. *ACS Appl. Mater. Interfaces* **2020**, *12*, 4895–4905.

[48] Das, P.; Wu, Z. S. MXene for energy storage: Present status and future perspectives. *J. Phys. Energy* **2020**, *2*, 032004.

[49] Zhang, Z. M.; Wei, Z. X.; Wan, M. X. Nanostructures of polyaniline doped with inorganic acids. *Macromolecules* **2002**, *35*, 5937–5942.

[50] Xie, W. H.; Yao, F. C.; Gu, H. B.; Du, A.; Lei, Q.; Naik, N.; Guo, Z. H. Magnetoresistive and piezoresistive polyaniline nanoarrays *in-situ* polymerized surrounding magnetic graphene aerogel. *Adv. Compos. Hybrid. Mater.* **2022**, *5*, 1003–1016.

[51] Ahirrao, D. J.; Jha, N. Comparative study on the electrosorption properties of carbon fabric, functionalized multiwall carbon nanotubes and solar-reduced graphene oxide for flow through electrode based desalination studies. *Carbon* **2019**, *152*, 837–850.

[52] Ansari, M. O.; Ansari, S. P.; Yadav, S. K.; Anwer, T.; Cho, M. H.; Mohammad, F. Ammonia vapor sensing and electrical properties of fibrous multi-walled carbon nanotube/polyaniline nanocomposites prepared in presence of cetyl-trimethylammonium bromide. *J. Ind. Eng. Chem.* **2014**, *20*, 2010–2017.

[53] Wu, D.; Yu, C. Y.; Zhong, W. B. Bioinspired strengthening and toughening of carbon nanotube@polyaniline/graphene film using electroactive biomass as glue for flexible supercapacitors with high rate performance and volumetric capacitance, and low-temperature tolerance. *J. Mater. Chem. A* **2021**, *9*, 18356–18368.

[54] Yoon, S. B.; Yoon, E. H.; Kim, K. B. Electrochemical properties of leucoemeraldine, emeraldine, and pernigraniline forms of polyaniline/multi-wall carbon nanotube nanocomposites for supercapacitor applications. *J. Power Sources* **2011**, *196*, 10791–10797.

[55] Korent, A.; Soderžnik, K. Ž.; Šturm, S.; Rožman, K. Z. A correlative study of polyaniline electropolymerization and its electrochromic behavior. *J. Electrochem. Soc.* **2020**, *167*, 106504.

[56] Zhong, M.; Song, Y.; Li, Y. F.; Ma, C.; Zhai, X. L.; Shi, J. L.; Guo, Q. G.; Liu, L. Effect of reduced graphene oxide on the properties of an activated carbon cloth/polyaniline flexible electrode for supercapacitor application. *J. Power Sources* **2012**, *217*, 6–12.

[57] Hosseini, M. G.; Shahryari, E. A novel high-performance supercapacitor based on chitosan/graphene oxide-MWCNT/polyaniline. *J. Colloid Interface Sci.* **2017**, *496*, 371–381.

[58] Zhou, Q. Q.; Li, Y. R.; Huang, L.; Li, C.; Shi, G. Q. Three-dimensional porous graphene/polyaniline composites for high-rate electrochemical capacitors. *J. Mater. Chem. A* **2014**, *2*, 17489–17494.

[59] Kulkarni, S. B.; Patil, U. M.; Shackery, I.; Sohn, J. S.; Lee, S.; Park, B.; Jun, S. High-performance supercapacitor electrode based on a polyaniline nanofibers/3D graphene framework as an efficient charge transporter. *J. Mater. Chem. A* **2014**, *2*, 4989–4998.

[60] Xing, J.; Liao, M. Y.; Zhang, C.; Yin, M.; Li, D. D.; Song, Y. The effect of anions on the electrochemical properties of polyaniline for supercapacitors. *Phys. Chem. Chem. Phys.* **2017**, *19*, 14030–14041.

[61] Cong, H. P.; Ren, X. C.; Wang, P.; Yu, S. H. Flexible graphene-polyaniline composite paper for high-performance supercapacitor. *Energy Environ. Sci.* **2013**, *6*, 1185–1191.

[62] Luo, H.; Wang, B.; Wang, F.; Yang, J.; Wu, F. D.; Ning, Y.; Zhou, Y.; Wang, D. L.; Liu, H. K.; Dou, S. X. Anodic oxidation strategy toward structure-optimized V$_2$O$_3$ cathode via electrolyte regulation for Zn-ion storage. *ACS Nano* **2020**, *14*, 7328–7337.

[63] Pu, L. Y.; Zhang, J. X.; Jiresse, N. K. L.; Gao, Y. F.; Zhou, H. J.; Naik, N.; Gao, P.; Guo, Z. H. N-doped MXene derived from chitosan for the highly effective electrochemical properties as supercapacitor. *Adv. Compos. Hybrid. Mater.* **2022**, *5*, 356–369.

[64] Pan, Z. H.; Cao, F.; Hu, X.; Ji, X. H. A facile method for synthesizing CuS decorated Ti$_3$C$_2$ MXene with enhanced performance for asymmetric supercapacitors. *J. Mater. Chem. A* **2019**, *7*, 8984–8992.

[65] Jiang, Q.; Kurra, N.; Alhabeb, M.; Gogotsi, Y.; Alshareef, H. N. All pseudocapacitive MXene-RuO$_2$ asymmetric supercapacitors. *Adv. Energy Mater.* **2018**, *8*, 1703043.

[66] Boota, M.; Gogotsi, Y. MXene-conducting polymer asymmetric pseudocapacitors. *Adv. Energy Mater.* **2019**, *9*, 1802917.

[67] Wang, X. W.; Zhang, D. Z.; Zhang, H. B.; Gong, L. K.; Yang, Y.; Zhao, W. H.; Yu, S. J.; Yin, Y. D.; Sun, D. F. *In situ* polymerized polyaniline/MXene (V$_2$C) as building blocks of supercapacitor and ammonia sensor self-powered by electromagnetic-triboelectric hybrid generator. *Nano Energy* **2021**, *88*, 106242.

[68] Boota, M.; Becuwe, M.; Gogotsi, Y. Phenothiazine-MXene aqueous asymmetric pseudocapacitors. *ACS Appl. Energy Mater.* **2020**, *3*, 3144–3149.

[69] Navarro-Suárez, A. M.; Van Aken, K. L.; Mathis, T.; Makaryan, T.; Yan, J.; Carretero-González, J.; Rojo, T.; Gogotsi, Y. Development of asymmetric supercapacitors with titanium carbide-reduced graphene oxide couples as electrodes. *Electrochim. Acta* **2018**, *259*, 752–761.

[70] Yan, J.; Ren, C. E.; Maleski, K.; Hatter, C. B.; Anasori, B.; Urbankowski, P.; Sarycheva, A.; Gogotsi, Y. Flexible MXene/graphene films for ultrafast supercapacitors with outstanding volumetric capacitance. *Adv. Funct. Mater.* **2017**, *27*, 1701264.

[71] Wang, X.; Li, H.; Li, H.; Lin, S.; Ding, W.; Zhu, X. G.; Sheng, Z. G.; Wang, H.; Zhu, X. B.; Sun, Y. P. 2D/2D 1T-MoS$_2$/Ti$_3$C$_2$ MXene heterostructure with excellent supercapacitor performance. *Adv. Funct. Mater.* **2020**, *30*, 0190302.

[72] Pan, Z. H.; Ji, X. H. Facile synthesis of nitrogen and oxygen co-doped C@Ti$_3$C$_2$ MXene for high performance symmetric supercapacitors. *J. Power Sources* **2019**, *439*, 227068.

[73] Zhou, H.; Lu, Y.; Wu, F.; Fang, L.; Luo, H. J.; Zhang, Y. X.; Zhou, M. MnO$_2$ nanorods/MXene/CC composite electrode for flexible supercapacitors with enhanced electrochemical performance. *J. Alloys Compd.* **2019**, *802*, 259–268.

[74] Boota, M.; Rajesh, M.; Bécuwe, M. Multi-electron redox asymmetric supercapacitors based on quinone-coupled viologen derivatives and Ti$_3$C$_2$T$_x$ MXene. *Mater. Today Energy* **2020**, *18*, 100532.

[75] Liu, W. F.; Zheng, Y. F.; Zhang, Z.; Zhang, Y. N.; Wu, Y. H.; Gao, H. X.; Su, J.; Gao, Y. H. Ultrahigh gravimetric and volumetric capacitance in Ti$_3$C$_2$T$_x$ MXene negative electrode enabled by surface modification and *in-situ* intercalation. *J. Power Sources* **2022**, *521*, 230965.

[76] Wu, W. L.; Wang, C. W.; Zhao, C. H.; Wei, D.; Zhu, J. F.; Xu, Y. L. Facile strategy of hollow polyaniline nanotubes supported on Ti$_3$C$_2$-MXene nanosheets for high-performance symmetric supercapacitors. *J. Colloid Interface Sci.* **2020**, *580*, 601–613.